Enhancing the teaching of seismic isolation using additive manufacturing

S. J. Calhoun[a], P. S. Harvey Jr.[a,*]

[a]*School of Civil Engineering and Environmental Science, University of Oklahoma, Norman, OK 73019, USA*

Abstract

This paper provides a complementary study to two previous papers by Virgin (2017a,b) [1, 2]. In those papers, 3D printing was used to provide hands-on experience for students studying structural analysis and structural dynamics, respectively. In this paper, the application of 3D printing is extended to investigate advanced seismic design strategies, namely seismic isolation. This paper describes the use of 3D printing to fabricate pendulum-type isolation bearings under parametric variation. Both sliding and rolling mechanisms are modeled, designed, fabricated and tested, and the influence of bearing geometry (radius) and damping (friction versus rolling resistance) on dynamic characteristics and isolation performance is explored.

Keywords: seismic isolation, rolling, sliding, pendulum, additive manufacturing, 3d printing

1. Introduction

Seismic isolation is a practical strategy for earthquake-resistant design whereby a flexible interface is introduced between the structure and its foundation [3, 4]. This has the result of lengthening the fundamental period of the structure, thus reducing the sustained accelerations in this mode and the earthquake-induced forces in the structure. Additive manufacturing (or 3D printing) offers compelling pedagogical opportunities in the context of learning seismic isolation. Pendulum-type isolators of simple geometry enable students to easily design, print, and test the isolation systems to verify isolation principles. The capabilities of 3D printing will allow for varied designs at a

---

*Corresponding author. Address: School of Civil Engineering and Environmental Science, University of Oklahoma, 202 W. Boyd St., Norman, OK 73019-1024, USA. Tel.: +1 405 325 3836

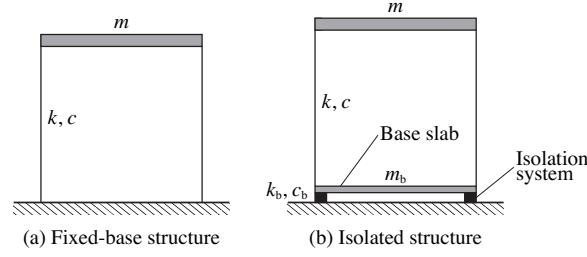*Email address:* harvey@ou.edu (P. S. Harvey Jr.)

Figure 1: Conceptual idealization of fixed-base (a) and isolated (b) structures.

lower cost compared to full-scale modeling. Varying the component geometries (e.g., curvature of the isolator) would allow for comparative studies that can be easily repeated, therefore allowing the student the opportunity to observe and compare theoretical calculations to empirical data. This paper provides a complementary study to previous papers by Virgin addressing structural analysis [1] and structural dynamics [2].

1.1. Basic theory of seismic isolation

In active seismic areas, buildings and their contents are susceptible to harmful vibrations from earthquake ground motions, posing a threat to the structural integrity of buildings and damage to sensitive equipment. Consider the fixed-base building shown in Fig. 1(a), which has lumped mass m, damping coefficient c, and lateral stiffness k. The natural period of the fixed-base structure is given by

$$T_{\mathrm{f}} = \frac{2\pi}{\omega_{\mathrm{f}}} \quad \text{where} \quad \omega_{\mathrm{f}} = \sqrt{\frac{k}{m}} \tag{1}$$

The natural period calculated from this equation, together with the damping ratio $\zeta_{\mathrm{f}} = c/(2\sqrt{km})$, is used to determine the pseudo-acceleration and hence earthquake-induced forces in the structure from elastic design spectra (Fig. 2). The fundamental period of low- to medium-rise buildings is commonly in the range of periods where earthquake energy is strongest, giving rise to large spectral accelerations. These accelerations can be reduced if the structure is designed to be more flexible (longer period), but this approach may be neither feasible nor practical [5]. The necessary flexibility can be achieved by *base isolation*. Base isolation provides an alternative to the standard, fixed-base design of structures and may be cost efficient for new buildings in highly active seismic locations [6].
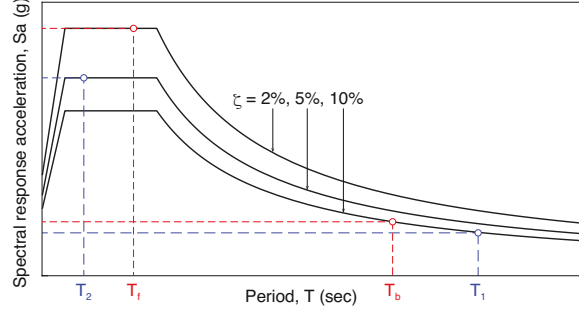
2

Figure 2: Elastic design spectra.

Consider the same *m*-*c*-*k* structure from before but now mounted on a base slab of mass m_b supported by isolation bearings [Fig. 1(b)]. The isolation system has lateral stiffness k_b and damping coefficient c_b. The period of the isolation system, assuming the building to be rigid, is given by

$$T_b = \frac{2\pi}{\omega_b} \quad \text{where} \quad \omega_b = \sqrt{\frac{k_b}{m + m_b}} \tag{2}$$

The base isolation period T_b must be much longer than the fixed-base period T_f in order to be effective in reducing the spectral accelerations and as a result the forces in the building. The two-degree-of-freedom system that defines the isolated structure [Fig. 1(b)] has two natural periods (T_1, T_2) that are close to, but do not exactly match, the fixed-base period T_f and isolation period T_b. The periods of the coupled system are given by

$$T_1 = \frac{2\pi}{\omega_1} \quad \text{and} \quad T_2 = \frac{2\pi}{\omega_2} \tag{3}$$

where the natural frequencies are found from the following equation [7]:

$$\omega_{1,2}^2 = \frac{1}{2(1 - \gamma)}\left[\omega_b^2 + \omega_f^2 \mp \sqrt{(\omega_b^2 - \omega_f^2)^2 + 4\gamma\omega_b^2\omega_f^2}\right] \tag{4}$$

in which the mass ratio γ is defined as

$$\gamma = \frac{m}{m + m_b} \tag{5}$$

Fig. 3 shows the influence of γ and the period ratio on the coupled system's modal periods.

The first mode is called the *isolation mode* because the isolation system undergoes deformations but the structure behaves as essentially rigid. The second mode is called the *structural mode*
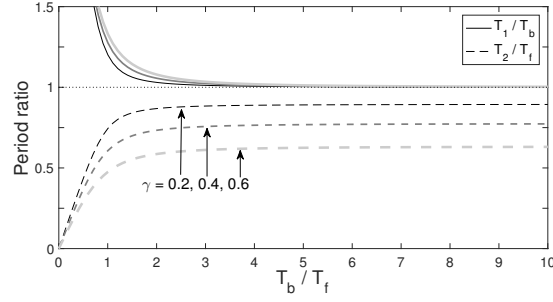
3

Figure 3: Effect of mass ratio γ and uncoupled period ratio T_b/T_f on the coupled system's natural periods T_1 and T_2.

because the it involves deformation of the structure as well as the isolation system. While the structural mode's pseudo-acceleration may be large (Fig. 2), this mode is essentially not excited [6] and contributes little to the earthquake-induced forces in the structure. The earthquake-induced forces are dominated by the fundamental (isolation) mode, which has low pseudo-accelerations (Fig. 2). Further, these forces are carried by the isolation bearings because the isolation mode involves deformations primarily in the isolation system. Hence the primary benefit of base isolation is the lengthening of the fundamental period, reducing earthquake-induced forces in the building. A secondary benefit of base isolation is the reduction in structural response through the damping in the isolation system [7].

1.2. Seismic isolation in practice

In practice, two types of isolation systems are commonly used. The first type involves the use of a flexible layer between the base of the structure and its foundation. The most common system of this type is laminated rubber bearings (LRB). These are short, cylindrical bearings with alternating layers of steel plates and hard rubber to remain vertically stiff yet horizontally flexible [8]. The addition of damping is readily incorporated through mechanical dampers such as hydraulic dampers, steel dampers, or a lead core [9].

The second type entails placing a pendulum mechanism between the foundation and the base of the structure. The most common system of this type is the *friction pendulum bearing* that operates through a sliding mechanism [10, 11]. The sliding interface provides enough friction to withstand strong winds and small earthquakes, while having a low coefficient of friction to dissipate shear forces created from large earthquakes. The sliding displacement is limited by curved sliding sur-

4

faces that provide a restoring force to return the bearing to its equilibrium position. In particular, the friction pendulum sliding bearing employs spherical sliding surfaces that slide relative to each other when the ground motion overcomes the static friction. When sliding occurs along the spherical surfaces, the building raises slightly resulting in gravitational restoring forces. Another type of pendulum bearing is the *rolling pendulum bearing*, which operates under the same gravitational restoring action [12]. These systems tend to have much less damping then their sliding counterparts due to the rolling resistance being much less than friction in sliding bearings [13]. For the purpose of this study, the isolation systems of interest are limited to rolling and sliding systems.

2. 3D Printing of Seismic Isolation Bearings

3D printing has increasingly been used as a teaching and research tool in mechanical engineering [14], revolutionizing the prototyping of mechanical components such as gears. More recently, 3D printing has been used to teach linear structural analysis [1] and structural dynamics [2] in the context of civil engineering. Thus, 3D printing has the capabilities of being used to teach base isolation, merging efforts from across mechanical and civil engineering disciplines. We shall focus attention on planar, pendulum-type isolation bearings supporting a single-degree-of-freedom planar frame structure. Two mechanisms are considered for the isolation bearings: sliding and rolling. These mechanisms were chosen partly to facilitate 3D printing, but also due to their ubiquity in practice. We shall focus attention on relatively simple geometries, as discussed in the following section, to obtain linear force-displacement relationships, but more complex geometries are discussed later.

2.1. Isolation Bearing Design and Fabrication

In this study, we consider two typical pendulum-type isolation bearings: friction pendulum (FP) bearings and rolling pendulum (RP) bearings. Fig. 4 shows the design for the FP bearing, which was modeled after a common design in practice [15]. The bearing is comprised of a bottom plate with circular sliding surface of radius R that is attached to the ground, an upper plate that supports the structure, and an articulated slider that transfers the load between the sliding surface and the upper plate. Fig. 5 shows the design for the RP bearing, which is comprised of lower
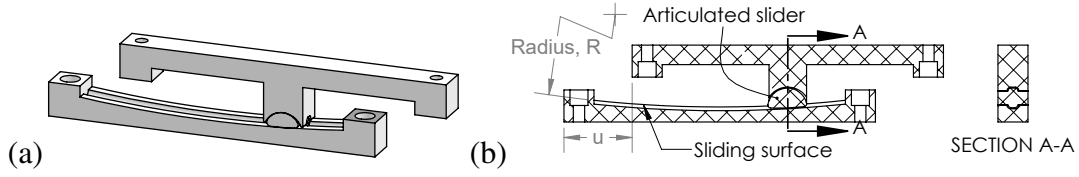
5

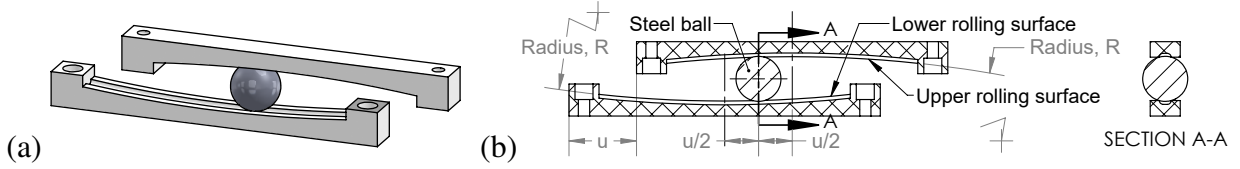Figure 4: Friction pendulum bearing schematic.

Figure 5: Rolling pendulum bearing schematic.

and upper rolling surfaces (both of radius R) and a steel ball interposed therebetween. Both of these bearings function under a pendulum-like mechanism, whereby horizontal translations result in vertical motion generating a gravitational restoring force. More details on modeling of these bearings will be given later.

In addition to varying the isolation mechanism, the bearing radius R provided parametric variation. Two radii were fabricated and tested: R = 254 and 508 mm. More specific details will be given on the selection of these two values in Section 3. The sliding and rolling surfaces were designed to be interchangeable to reduce the number of surfaces that needed to be printed. Details of the sliding/rolling surfaces are shown in Fig. 6. The surfaces had a center line groove that accommodated the articulated slider (that had a matching tongue; Fig. 7) and the 19.1-mm steel ball (not shown), which provided resistance transverse to the bearing's intended motion. The radii of the articulated slider were selected so as to avoid binding both laterally and longitudinally. A matching groove in the upper mount of the FP bearing (Fig. 8) was designed to allow the slider to articulate. To keep the bearing profile as thin as possible, the bearings were designed with recessed bolt holes leaving enough clearance to avoid contact at zero displacement. For the bearing component designs, the nominal displacement capacities of the FP and RP bearings are 44 and 89 mm, respectively.

The bearing components were fabricated using a relatively inexpensive 3D printer (Taz 6, LulzBot, Loveland, CO). Polylactic acid (PLA) thermoplastic was used because it tends to be more
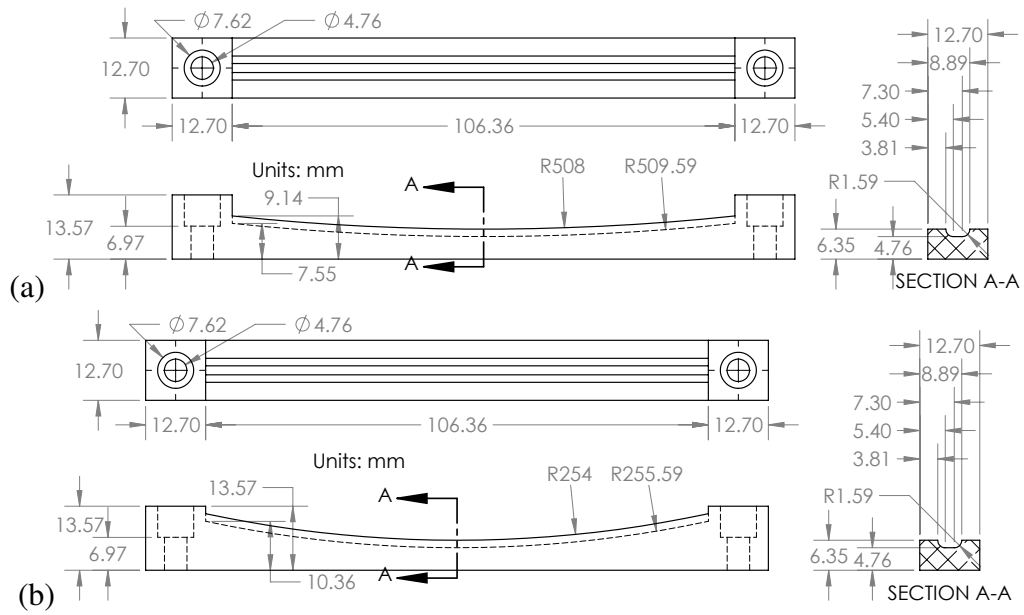
6

Figure 6: Details of sliding/rolling surfaces used in FP/RP bearings with R = (a) 508 mm and (b) 254 mm.
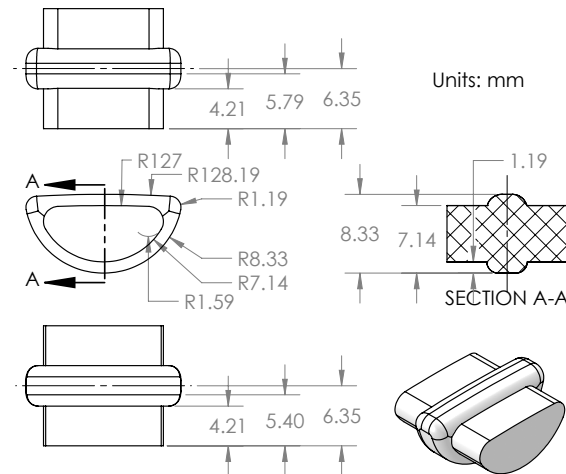

Figure 7: Details of articulated slider used in FB bearings.

forgiving and show less warping from differential cooling than acrylonitrile butadiene styrene (ABS) thermoplastics. The 3D printer has a heated print surface to further reduce the warping. Warping was of particular concern because it would lead to misalignment in the bearings.
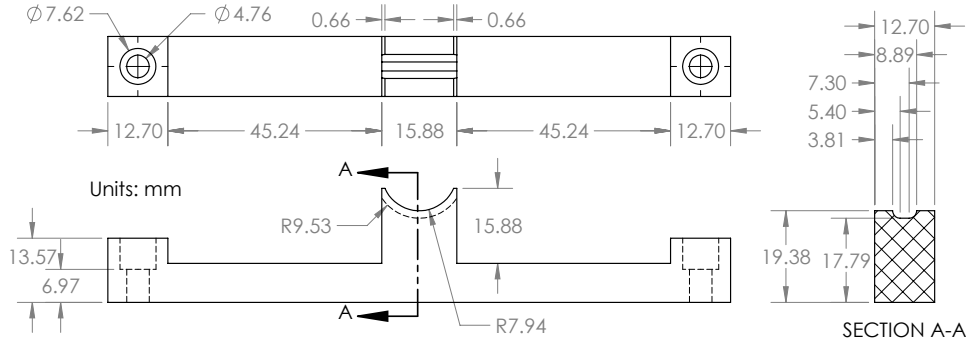
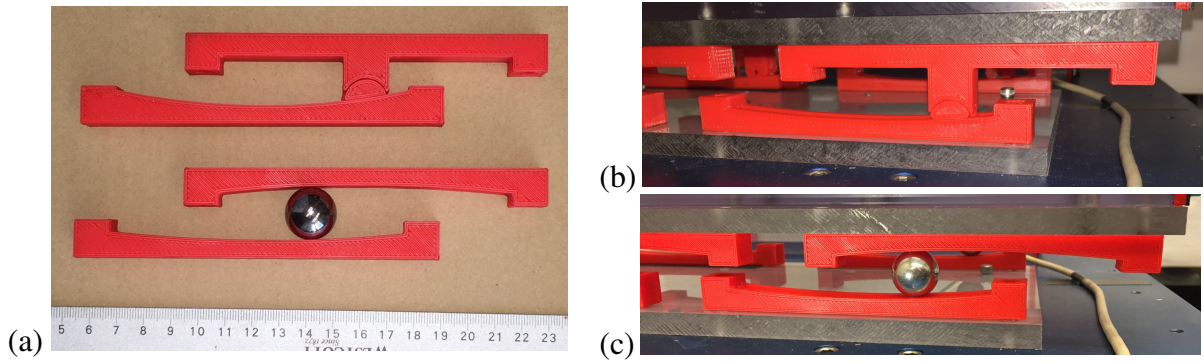Figure 8: Details of upper mount for FB bearing.

Figure 9: (a) Printed friction pendulum (top) and rolling pendulum (bottom) bearings. Assembled isolation bearings: (b) friction pendulum bearing; (c) rolling pendulum bearing.

2.2. System Assembly and Setup

For the experimental system, a single-story shear-type building model was isolated using the 3D printed bearings. The fabricated bearing components are shown in Fig. 9(a), and the assembled isolation bearings are shown in Figs. 9(b) and 9(c). The isolation layer was assembled from two 152.4 mm × 304.8 mm polycarbonate plates to which four bearings were attached at the corners. The bottom plate was bolted to a single-axis shake table, and the top plate was bolted to the base of the building model. The base slab mass m_b is approximately 1.24 kg, which includes the upper bearing elements, the top plate, the base of the building model, one accelerometer, half the column masses, and mounting hardware. The structure mass m is approximately 0.677 kg, which includes the roof of the building model, an accelerometer, and half the column masses.

To reduce friction and wear in the FP bearings, a wet lubricant (petrolatum) was applied to the sliding surfaces. Quasi-static inclination tests were conducted to determine the static coeffi-
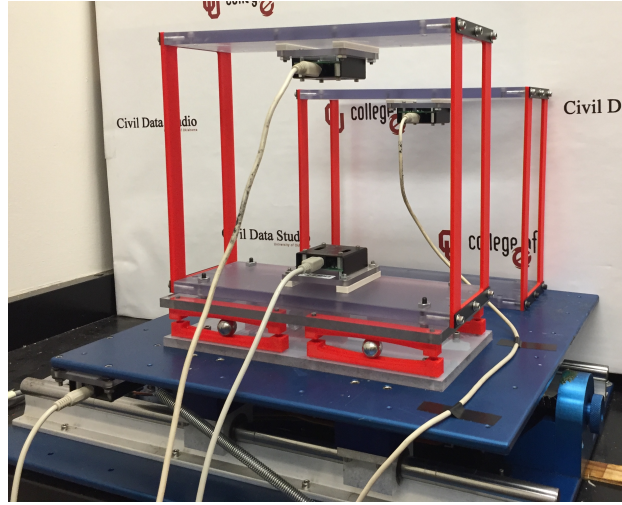
8

Figure 10: The experimental test setup. Isolated structure in foreground, with the fixed-base structure in the background. Both are attached to the shake table. Accelerometers are attached to the shake table, above the the isolation layer, and to the roofs of both structures.

cient of friction. Motion was initiated at an incline of approximately 15°, which corresponds to a static coefficient of friction of 0.27. While this is substantially higher than traditional ranges for friction coefficient in self-lubricating bearing surfaces (0.05 – 0.15) [16, 17], other researchers have recently explored low-cost, high-friction (0.15 – 0.25) FP bearings as an approach to significantly decrease required design displacements [18, 19]. These 3D fabricated bearings, therefore, are more representative of the latter. It is worth noting that such a high coefficient of friction will affect the sliding isolation performance, as shown later.

Fig. 10 shows the experimental setup. A second structure was attached directly to the shake table to serve as a point of comparison between base isolated and fixed-base buildings subject to an earthquake.

Experiments were conducted on a Quanser Shake Table II (Markham, Ontario, Canada). The Quanser table was acquired through the University Consortium on Instructional Shake Tables [20], which was was developed to enhance undergraduate and graduate education in earthquake engineering. The table can achieve a peak acceleration of 2.5 g and has a stroke of ±75 mm. The table was controlled in *Simulink* through *QUARC* real-time control software.

An array of accelerometers was installed on the experimental system. Four accelerometers

(ADXL210E, Alldata, Elk Grove, California) were installed to measure acceleration in the x direction (horizontal): one mounted underneath the stage to measure the acceleration of the shake table, one mounted immediately above the isolation layer to measure the acceleration across the isolation system, and one mounted to to roof of each structure to measure the roof acceleration. Accelerations were acquired at 1 kHz.

The rest of this paper seeks to establish natural periods of the pendulum bearings and their geometric parameter dependence, as well as their seismic isolation performance. The goal here is to exploit the versatility of 3D printing for deepening an appreciate for seismic isolation. This practical component can be used to enhance the understanding of linear structural dynamics, earthquake engineering, and vibrations in general.

3. Basic Modeling

A basic model for the isolation systems can be developed via Lagrange's equation. Assuming that the building is rigid relative to the isolation system, the kinetic energy, in terms of the total mass $M = m + m_b$, is $\mathcal{T} = \frac{1}{2} M (\dot{u}_g + \dot{u})^2$ where $u_g(t)$ is the horizontal ground displacement, $u(t)$ is the horizontal displacement across the isolation bearings, and the overdot means differentiation with respect to time, i.e., $\dot{u} \equiv du/dt$. We have assumed that the vertical kinetic energy is negligible due to the shallow sliding/rolling surface profiles. Further, we have neglected the kinetic energy associated with the rolling balls.

The potential energy in the system is given entirely by the gravitational potential energy $\mathcal{V} = Mgh(u)$, i.e., assuming the building to be rigid and neglecting strain energy stored in the building columns. The height $h(u)$ is dictated by the sliding/rolling surface profile, with the functional form for $h(u)$ depending on the specific isolation bearing type. For the friction pendulum bearing, the height is given by the surface profile elevation at the articulated slider which displaces the same amount as the mass (Fig. 4). For the rolling pendulum bearing, the height is given by two times the surface profile elevation at the ball which is half the displacement across the bearing (Fig. 5). Assuming a circular profile, the elevation is given by

$$y(x) = R - \sqrt{R^2 - x^2} \tag{6}$$

10

Hence, the height is given by

$$h(u) = \begin{cases} y(u), & \text{friction pendulum bearing} \\ 2y(u/2), & \text{rolling pendulum bearing} \end{cases} \tag{7}$$

The equation of motion is given, via Lagrange's equation, by the second-order differential equation

$$M\ddot{u} + c\dot{u} + f + Mgh'(u) = -M\ddot{u}_{\text{g}} \tag{8}$$

where c is the linear viscous damping coefficient and f is the friction force. The friction may be modeled as the Coulomb friction [21], and f is taken to be $f = \mu Mg\, \text{sgn}(\dot{u})$ where μ is the coefficient of friction. The gravitational restoring force $Mgh'(u)$ depends on the gradient of the assumed profile [Eq. (6)] through the height function [Eq. (7)]. The derivative $y'(x)$ can be simplified by retaining the linear term in its Taylor series expansion:

$$y'(x) = \frac{x}{\sqrt{R^2 - x^2}} \approx \frac{x}{R} \tag{9}$$

Upon substituting this expression into the height function [Eq. (7)], the (linearized) gravitational restoring force is recovered:

$$Mgh'(u) = \begin{cases} Mg\dfrac{u}{R}, & \text{friction pendulum bearing} \\ Mg\dfrac{u}{2R}, & \text{rolling pendulum bearing} \end{cases} \tag{10}$$

It is immediately apparent that the stiffness is mass proportional, and the natural frequency, therefore, is independent of the mass, as it is in the case of a pendulum. Furthermore, the stiffness is inversely proportional to the radius of curvature, R. The linearized natural periods of the two bearing mechanisms are given by

$$T_{\text{b}} = \begin{cases} 2\pi\sqrt{R/g}, & \text{friction pendulum bearing} \\ 2\pi\sqrt{2R/g}, & \text{rolling pendulum bearing} \end{cases} \tag{11}$$

Table 1 gives the theoretical natural periods for the two radii considered. Note that for the two different mechanisms (sliding and rolling), the natural periods are different for the same radius R.

11

Table 1: Isolation bearing geometries and results from free response system identification. Fixed-base structure period $T_f = 0.182$ s.

Type	R [mm]	Theoretical[1]			Experimental		
		T_b [s]	T_1 [s]	T_2 [s]	T_b [s]	T_1 [s]	T_2 [s]
Sliding	508	1.43	1.43	0.146	–	–	–
	254	1.01	1.02	0.146	–	–	–
Rolling	508	2.02	2.03	0.146	1.97	2.00	0.154
	254	1.43	1.43	0.146	1.41	1.42	0.156

[1]For mass ratio $\gamma = 0.353$.

This is due to the factor of 2 in the denominator of the restoring force [Eq. (10)] for the rolling pendulum bearing, which is present because of the kinematics of the rolling ball that moves half the total displacement across the bearing.

Assuming a natural period of the fixed-base structure alone of 0.182 s (the experimentally determined T_f described later), Eq. (4) can be used in conjunction with Eq. (3) to determine the natural periods of the coupled system. Table 1 gives the theoretical values for T_1 and T_2 for a mass ratio $\gamma = 0.353$ (the value determined for the experimental setup described before). The isolation period T_1 lengthens very little from the isolation system period T_b, while the structural period is shortened by about 25%.

4. Results

For this study the main emphasis is on the effect of the isolation bearing mechanism (sliding/rolling) and of geometric changes (radius) on the isolation system's behavior and ultimately performance. Free vibration tests were first conducted to identify the experimental system properties, and then the systems were subjected to earthquake ground motions to evaluate the seismic isolation performance.
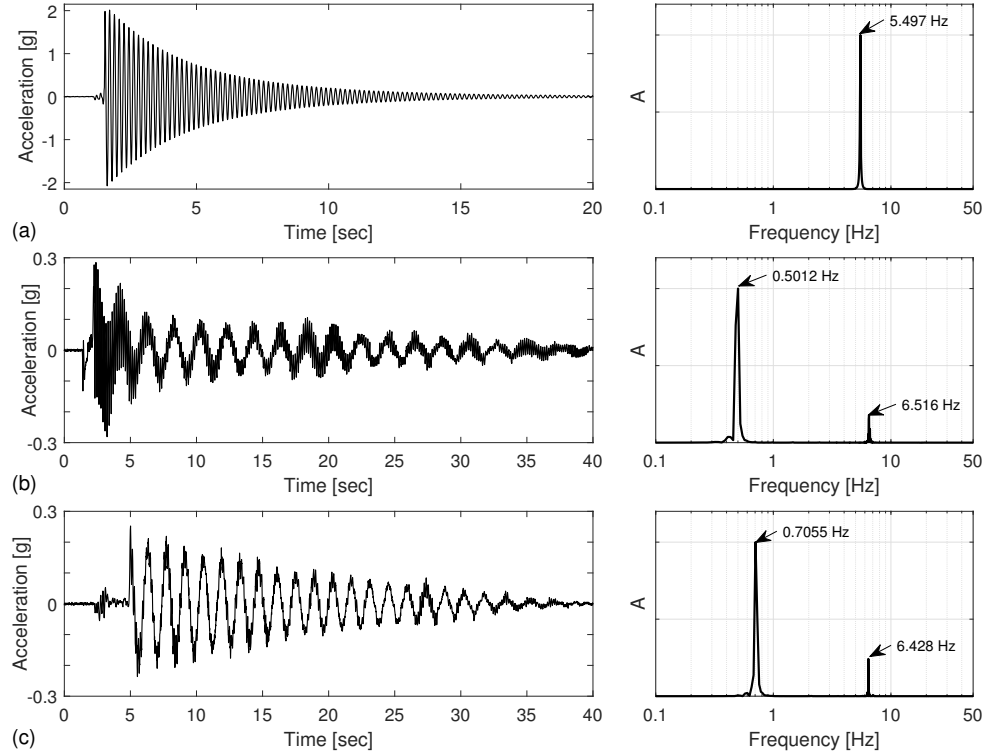
Figure 11: Free responses of the (a) fixed-base structure and the isolated building—(b) 508-mm RPS and (c) 254-mm RPS—and the corresponding frequency content (FFT). *A* is in arbitrary units.

4.1. Free Vibration Tests

Free vibration tests were conducted to extract the natural periods of the fixed-base structure and isolated system. Motion for the free response tests was initiated by applying an initial deflection and then releasing, and the subsequent time series was recorded by the accelerometers. Gathered data was then subject to a spectral analysis and the natural periods extracted. In particular, the natural frequency was extracted using the fast Fourier transform (FFT) within Matlab. Fig. 11 shows the measured free decay time series and corresponding FFT spectra for (a) the fixed-base structure and (b,c) the structure isolated with the rolling pendulum system (RPS) with radius *R* = (b) 508 and (c) 254 mm. Note that the friction pendulum system (FPS) was not tested because the friction prevented any free vibration in the bearings.

For the fixed-base structure [Fig. 11(a)], the FFT gives a natural frequency of 5.497 Hz, corresponding to a period of 0.182 s (the value reported in Table 1 for the fixed-base structure). The

13

natural period can alternatively be determined by picking peaks over j cycles of motion and averaging the time to complete a cycle. Doing so confirms the period of oscillation of 0.182 s. Additionally, the damping ratio ζ_f can be determined from the decrease in acceleration amplitude from $\ddot{u}_i$ to $\ddot{u}_{i+j}$ over j cycles of motion [6]:

$$\zeta \approx \frac{1}{2\pi j} \ln \left(\frac{\ddot{u}_i}{\ddot{u}_{i+j}} \right) \tag{12}$$

Using the logarithmic decrement approach, the damping ratio for the fixed-base structure was found to be 0.82%, confirming that the structure is very lightly damped.

For the isolated structures [Figs. 11(b) and 11(c)], two distinct frequencies can be observed in the time series and FFT, which correspond to the isolation and structural modes. For the RPS with radius R = 508 mm [Fig. 11(b)], the FFT gives natural frequencies of 0.5012 and 6.516 Hz, or natural periods of 2.00 and 0.154 s. The former is the fundamental period of the system, the isolation mode, where the structure remains effectively rigid. This value closely matches the theoretical value (Table 1). The latter is the structural mode, which involves deformation of the structure as well as the isolation system. The value is sightly shorter than that of the fixed-base structure due to the frequency splitting phenomena caused by coupling the building to the isolation system. Good agreement is observed between the theoretical and experimental isolation and structural periods.

A similar behavior appears for the the 254 mm rolling isolation system. Fig. 11(c) shows the response of the 254-mm RPS and the isolated and structural frequencies 0.7055 and 6.428 Hz, respectively. The isolated frequency is close to the theoretical value of 0.707 Hz. It appears to be a decrease in the structural frequency value. Table 1 summarizes the theoretical and experimental free responses described above.

In addition to the free vibration tests of the isolated system (i.e., the isolated SDOF structure), free vibration tests were conducted on the isolation system alone by replacing the structure with rigid blocks. The free responses (not shows) gave base isolation periods T_b of 1.97 and 1.41 s for the RPSs with radius R = 508 and 254 mm, respectively. These values are also reported in Table 1. As predicted theoretically, the base isolation period is shorter than the isolation period in the coupled system.

14

4.2. Earthquake Tests

Next, the earthquake response of the fixed-base building and isolated building with FP and RP bearings was examined to assess the seismic isolation performance. For the dynamic earthquake testing, we consider three earthquake records, which are listed in Table 2. The earthquake records were scaled in length and time to meet the limitations of the shake table. The time and length scale factors, peak ground acceleration (PGA), and peak ground displacement (PGD) of each record (at the 100% amplitude) are listed in Table 2. Additional length scales are considered in the incremental dynamic analysis (Section 4.2.1).

The ground-motion time-histories are shown in Fig. 12 for the three earthquake records (at the 100% amplitude). Additionally, acceleration response spectra are shown for damping ratios of $\zeta = 0.5$, 1 and 5 %. The vertical lines indicate the periods of interest for the experimental system: fixed-base period, $T_f = 0.18$ s; base isolation periods, $T_b = 2$ and 1.4 s; and structural-mode period of the isolated system, $T_2 = 0.15$ s. Note that T_f and T_2 fall within the portion of the spectrum where the energy is strongest, whereas T_b is in the lower energy region (by design).

Figs. 13 and 14 show the response time histories for Kobe and Mendocino at the 100% amplitude. From these figures, it is immediately apparent that the roof acceleration is considerably reduced in the isolated cases when compared to the fixed-base building. For Kobe (Fig. 13), reductions on the order of 60% and 90% are observed for the FP and RP bearings, respectively. The damping in the FP bearing increases the coupling and decreases the isolation performance, whereas the RP bearing is very lightly damped leading to the dramatic reduction in accelerations. In fact, the RP bearing consistently isolates throughout the entire test, while there is a portion at

Table 2: Records used for earthquake tests.

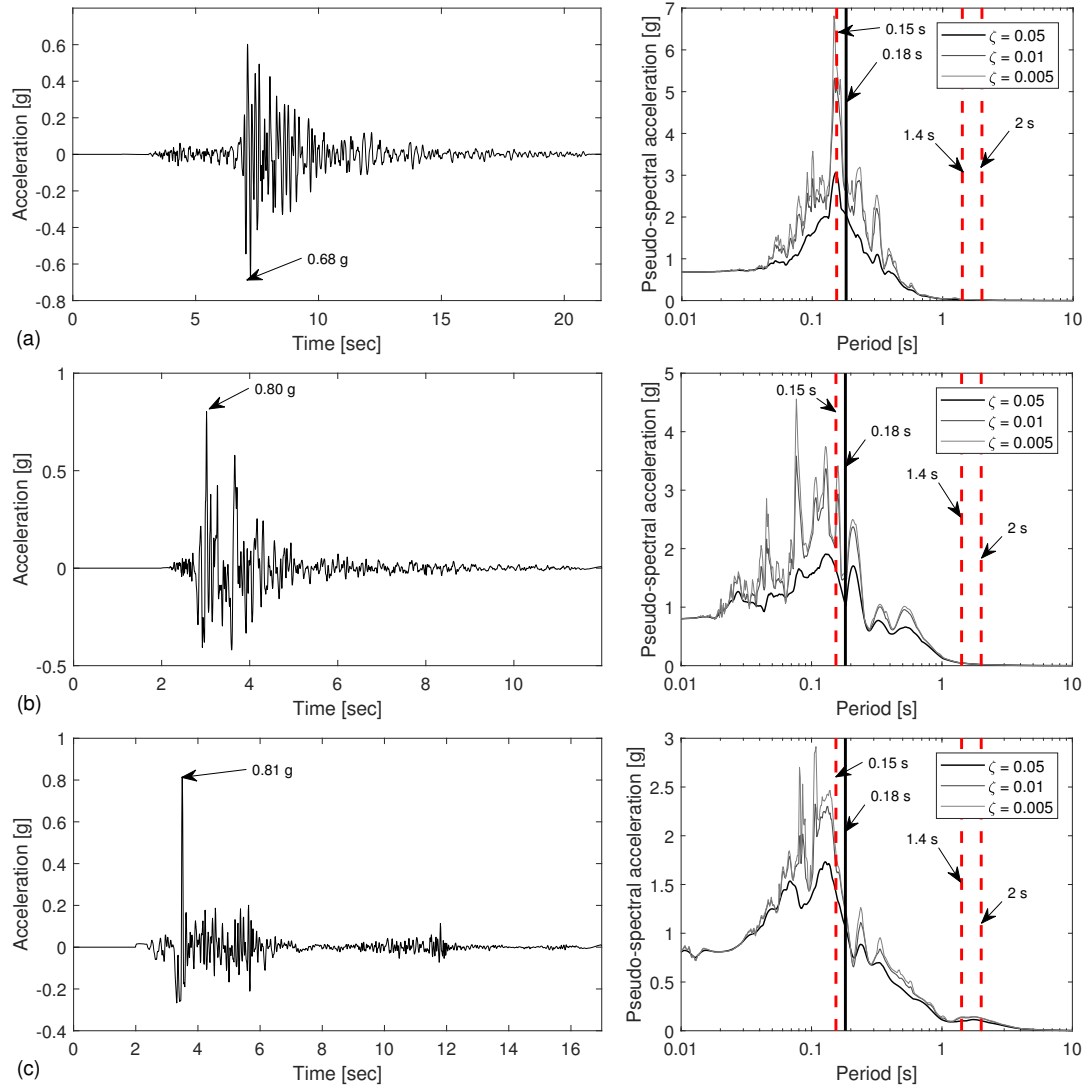| Event	Year	Station	Record	Time scale	Length scale	PGA [g]	PGD [mm]
Kobe	1995	HIK	HIK000	1/4	1/3.3	0.68	10
Northridge	1994	Sylmar - Hospital	SYL090	1/2	1/11	0.80	15
Cape Mendocino	1992	Cape Mendocino	CPM000	1/4	1/7.0	0.81	50

Figure 12: Time history of earthquakes used for evaluating the fixed base and isolation systems—(a) Kobe, (b) Northridge (c) Mendocino—and their corresponding frequency content (response spectra).

the beginning of the FP test in which the fixed-based and isolated buildings respond identically [e.g., time 0–7 s in Fig. 13(a)]. This corresponds to base shear insufficient to overcome the static friction in the sliding bearing, with the bearing acting as rigid; it is not until the ground accelerations become sufficiently large to overcome friction that bearing displacements are realized and isolation is achieved. Similar response behaviors and isolation performance were observed in the case of Northridge (not shown).

For Mendocino (Fig. 14), the FP bearings (a,c) exhibited similar performance as the Kobe
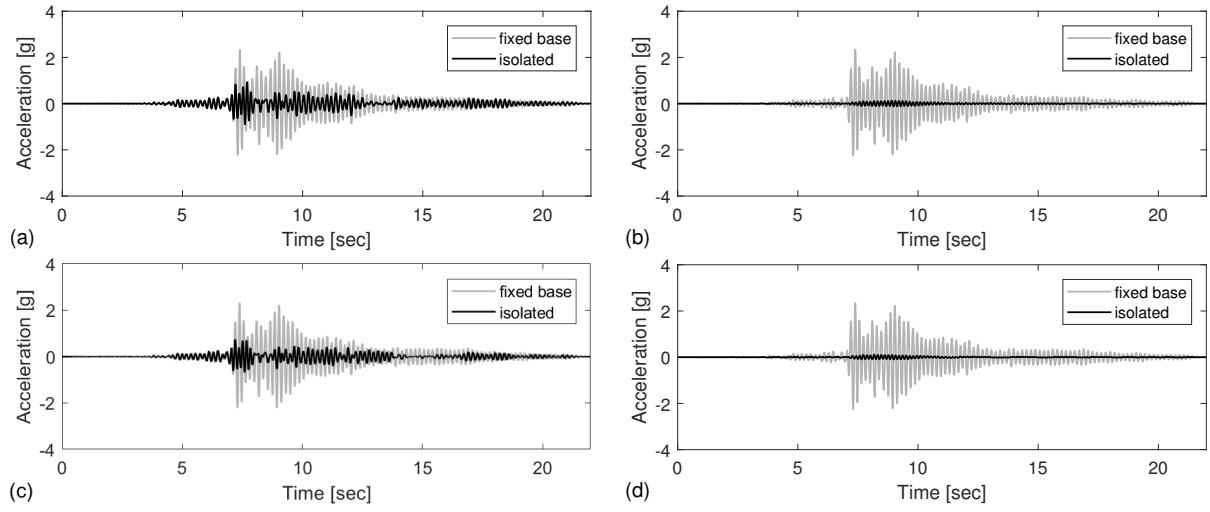
16

Figure 13: Roof acceleration response of fixed-base building and isolated buildings—(a) 254-mm FPS, (b) 508-mm RPS, (c) 508-mm FPS, and (d) 254-mm RPS—subjected to Kobe ground motion.
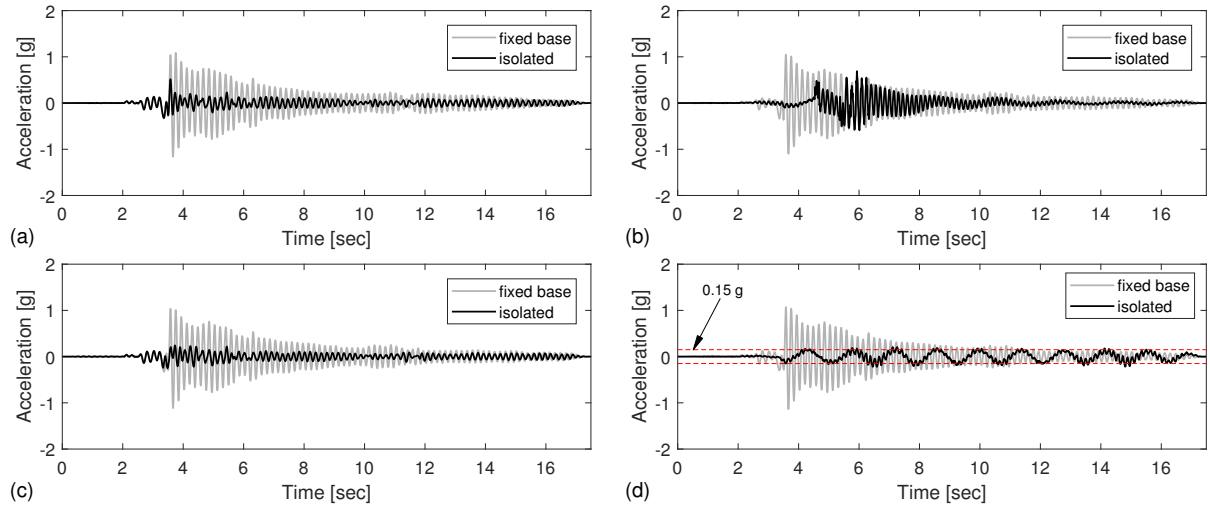

Figure 14: Roof acceleration response of fixed-base building and isolated buildings—(a) 254-mm FPS, (b) 508-mm RPS, (c) 508-mm FPS, and (d) 254-mm RPS—subjected to Mendocino ground motion.

event, but the RP bearing (b,d) exhibited much larger responses, with a distinct long-period component of the response at the isolation period (2.0 and 1.4 s, respectively). The reason for this large isolation response can be explained from the response spectra in Fig. 12. Above a period of 1 s, Kobe (a) and Northridge (b) have nearly zero pseudo-spectral acceleration, while Mendocino exhibits a long period component in the 1–2 s range where the isolation period is located.

The spectral acceleration at the isolation period is roughly 0.15 g, which matches the measured acceleration response for the 254-mm RPS indicated by the dashed line in Fig. 14(d); the 508-mm RPS [Fig. 14(d)] exhibited larger accelerations due to vibrations in the isolated building (i.e., with 6.5-Hz content). It is clear that the effectiveness of base isolation is diminished under long-period ground motions [22].

4.2.1. Incremental Dynamic Analysis

Finally, the behavior of the systems is assessed at multiple ground-motion amplitudes. In this *incremental dynamic analysis* [23], five to six ground-motion amplitudes are considered for each earthquake, and peak responses are recorded for the fixed-base building and isolated building with each bearing. By making incremental changes to the earthquake intensity, it is then possible to gain an appreciation for nonlinearities and their effect on the systems' behavior.

Fig. 15 show the peak roof accelerations versus PGA for (a) Kobe, (b) Northridge, and (c) Mendocino. These figures contain a wealth of information. First, the fixed-base structure behaves linearly as expected. With increasing PGA, the peak roof acceleration increases proportionately. This behavior is seen to be repeatable as well, as indicated by the four coincident markers at each PGA—one for each isolation configuration.

Second, the peak roof acceleration for the friction pendulum systems (FPSs) are identical to those of the fixed-base building for low PGAs. This is due to the base shear being insufficient to overcome static friction in the bearings, not allowing deflection across the bearing, resulting in an effectively fixed-base building. The critical PGA at which static friction is overcome and sliding in the bearing is initiated, is in the range (a) 0.136 – 0.272 g, (b) 0.268 – 0.401 g, and (c) 0.325 – 0.487 g. Neglecting any dynamic effects, the coefficient of static friction can be approximated by this critical PGA. Doing so, gives a value of about $\mu_s = 0.27$, which is consistent with the value determined through the quasi-static inclination tests. While this relatively high friction coefficient degrades the isolation performance, reductions in the peak roof acceleration of nearly 50% are observed at high PGAs. Even better isolation performance would be expected if a lower friction coefficient was achieved in the FP bearings (see Section 5).

Third, the rolling pendulum system (RPS) isolated effectively for all PGAs. This is due to
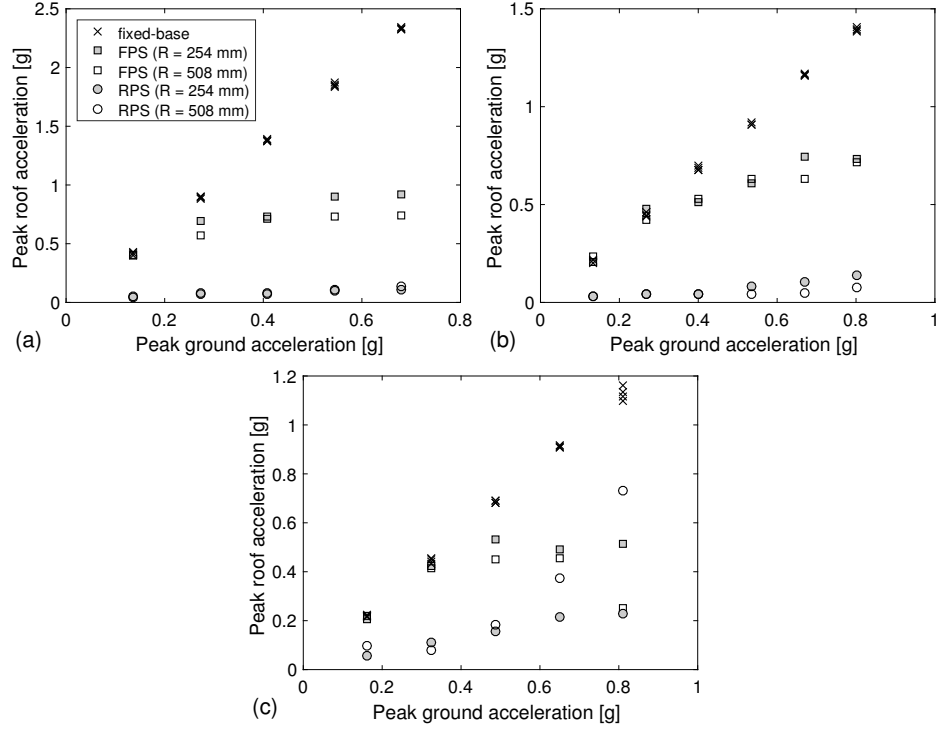
18

Figure 15: Incremental dynamic analysis. Peak roof acceleration versus peak ground acceleration for the fixed-base building and the building isolated using a friction pendulum system (FPS) or a rolling pendulum system (RPS) with varying radius R: (a) Kobe, (b) Northridge, and (c) Mendocino.

the very low rolling resistance in these systems. The worst performance for the RPS was for Mendocino [Fig. 15(c)], which is attributed to the long-period content as previously discussed.

Fourth, the radius had a slight influence on the isolation performance. For example, the acceleration response of the FPS with $R = 254$ mm under Kobe [Fig. 15(a)] is consistently larger than with $R = 508$ mm, which is suggested by Eq. (11) (i.e., smaller R means a shorter period closer to the portion of the response spectrum where the energy is strongest). Similar trends are observed for the RPS under Northridge [Fig. 15(b)].

5. Discussion and Other Practical Considerations

As demonstrated here, 3D printing has a potentially useful role to play in the teaching of earthquake engineering and seismic isolation. By making isolated but consistent parametric changes, which is easily accomplished in 3D printing, it is then possible to gain an appreciation for how

19

seismic isolation performance depends on the geometry of the isolation bearing, as well as the isolation mechanism. Considerations concerning failure limit states such as insufficient bearing capacity could also be addressed [24, 25], but were not considered here. Other extensions to this work can easily be envisioned, for example:

- Vary the surface geometry for nonlinear gravitational restoring forces, such as constant slope [26] and polynomial [27];

- Incorporate supplemental damping in the RP bearings, such as rubber balls or elastomeric liners [26];

- Explore means of reducing the friction coefficient in the FP bearings, such as using other wet lubricants (or a dry lubricant) or printing the sliding surfaces with a self-lubricating synthetic polymers (e.g., polytetrafloroethylene (PTFE) [28]);

- Consider more complex mechanisms, such as triple friction pendulum [29].

In addition to the benefits to teaching seismic isolation, 3D printing of isolation bearings has the potential to greatly enhance the testing of novel isolation bearing designs in research and practice.

6. Concluding Remarks

The teaching of advanced seismic design strategies, such as base isolation, typically relies on empirical techniques, analytic expressions and numerical simulation. Experimental demonstrations can provide a beneficial practical appreciation of these theoretical concepts, and 3D printing in particular can easily facilitate the construction and testing of isolation bearings. Making mechanical and geometric changes to bearing designs enables a direct comparative study to be conducted. Furthermore, students are given the opportunity to design, fabricate, and test their own bearings, permitting hands-on learning and a deeper appreciation for the concepts taught in the classroom. These concepts could easily be incorporated into inductive learning approaches in interactive classrooms [30].

References

[1] L. N. Virgin, Enhancing the teaching of linear structural analysis using additive manufacturing, Engineering Structures 150 (Supplement C) (2017) 135–142. `doi:10.1016/j.engstruct.2017.07.054`.

[2] L. N. Virgin, Enhancing the teaching of structural dynamics using additive manufacturing, Engineering Structures 152 (Supplement C) (2017) 750–757. `doi:10.1016/j.engstruct.2017.09.052`.

[3] I. G. Buckle, R. L. Mayes, Seismic isolation: History, application, and performance–a world view, Earthquake Spectra 6 (2) (1990) 161–201. `doi:10.1193/1.1585564`.

[4] J. M. Kelly, Aseismic base isolation: review and bibliography, Soil Dynamics and Earthquake Engineering 5 (4) (1986) 202 – 216. `doi:https://doi.org/10.1016/0267-7261(86)90006-0`.

[5] J. M. Kelly, Base isolation: Linear theory and design, Earthquake Spectra 6 (2) (1990) 223–244. `doi:10.1193/1.1585566`.

[6] A. K. Chopra, Dynamics of Structures: Theory and Applications to Earthquake Engineering, 4th Edition, Prentice Hall, Englewood Cliffs, New Jersey, 2012.

[7] J. M. Kelly, The role of damping in seismic isolation, Earthquake Engineering and Structural Dynamics 28 (1999) 3–20. `doi:10.1002/(SICI)1096-9845(199901)28:1<3::AID-EQE801>3.0.CO;2-D`.

[8] G. P. Warn, A. S. Whittaker, M. C. Constantinou, Vertical stiffness of elastomeric and lead-rubber seismic isolation bearings, Journal of Structural Engineering 133 (9) (2007) 1227–1236. `doi:10.1061/(ASCE)0733-9445(2007)133:9(1227)`.

[9] W. H. Robinson, Lead rubber hysteretic bearings suitable for protecting structures during earthquakes, Earthquake Engineering and Structural Dynamics 10 (1982) 593–604. `doi:10.1002/eqe.4290100408`.

[10] V. A. Zayas, S. S. Low, S. A. Mahin, A simple pendulum technique for achieving seismic isolation, Earthquake Spectra 6 (2) (1990) 317–333. `doi:10.1193/1.1585573`.

[11] R. S. Jangid, Optimum friction pendulum system for near-fault motions, Engineering Structures 27 (2005) 249–259. `doi:10.1016/j.engstruct.2004.09.013`.

[12] P. S. Harvey, Jr., K. C. Kelly, A review of rolling-type seismic isolation: Historical development and future directions, Engineering Structures 125 (2016) 521–531. `doi:10.1016/j.engstruct.2016.07.031`.

[13] P. S. Harvey, Jr., H. P. Gavin, The nonholonomic and chaotic nature of a rolling isolation system, Journal of Sound and Vibration 332 (2013) 3535–3551. `doi:10.1016/j.jsv.2013.01.036`.

[14] F. Pieterse, A. Nel, The advantages of 3D printing in undergraduate mechanical engineering research, in: 2016 IEEE Global Engineering Education Conference, Abu Dhabi, UAE, 2016, pp. 25–31. `doi:10.1109/EDUCON.2016.7474526`.

[15] G. Mosqueda, A. S. Whittaker, G. L. Fenves, Characterization and modeling of friction pendulum bearings subjected to multiple components of excitation, Journal of Structural Engineering 130(3) (2004) 433–442. `doi:10.1061/(ASCE)0733-9445(2004)130:3(433)`.

[16] M. C. Constantinou, J. Caccese, H. G. Harris, Frictional characteristics of teflon–steel interfaces under dynamic conditions, Earthquake Engineering & Structural Dynamics 15 (6) (1987) 751–759. `doi:10.1002/eqe.4290150607`.

[17] G. Bondonet, A. Filiatrault, Frictional response of ptfe sliding bearings at high frequencies, Journal of Bridge Engineering 2 (4) (1997) 139–148. `doi:10.1061/(ASCE)1084-0702(1997)2:4(139)`.

[18] E. A. Jampole, S. D. Swensen, B. Fell, E. Miranda, G. G. Deierlein, Dynamic testing of a low-cost sliding isolation system for light-frame residential structures, in: Proceedings of 10NCEE, Anchorage, AK, 2014.

[19] E. Jampole, G. Deierlein, E. Miranda, B. Fell, S. Swensen, C. Acevedo, Full-scale dynamic testing of a sliding seismically isolated unibody house, Earthquake Spectra 32 (4) (2016) 2245–2270. `doi:10.1193/010616EQS003M`.

[20] S. Dyke, J. Caicedo, M. Soto-Fournier, University consortium of instructional shake tables: Enhancing education in earthquake engineering, in: Proceedings of the International Meeting on Civil Engineering Education, Real Cuidad, Spain, 2003.

[21] J. L. Alma'an, J. C. De La Llera, J. A. Inaudi, Modelling aspects of structures isolated with the frictional pendulum system, Earthquake Engineering & Structural Dynamics 27 (8) (1998) 845–867. `doi:10.1002/(SICI)1096-9845(199808)27:8<845::AID-EQE760>3.0.CO;2-T`.

[22] E. Sato, S. Furukawa, A. Kakehi, M. Nakashima, Full-scale shaking table test for examination of safety and functionality of base-isolated medical facilities, Earthquake Engineering & Structural Dynamics 40 (13) (2011) 1435–1453. `doi:10.1002/eqe.1097`.

[23] D. Vamvatsikos, C. A. Cornell, Incremental dynamic analysis, Earthquake Engineering and Structural Dynamics 31 (3) (2002) 491–514. `doi:10.1002/eqe.141`.

[24] Y. Bao, T. C. Becker, H. Hamaguchi, Failure of double friction pendulum bearings under pulse-type motions, Earthquake Engineering & Structural Dynamics 46 (5) (2017) 715–732, eQE-15-0484.R2. `doi:10.1002/eqe.2827`.
    URL `http://dx.doi.org/10.1002/eqe.2827`

[25] M. Ismail, Inner pounding control of the RNC isolator and its impact on seismic isolation efficiency under near-fault earthquakes, Engineering Structures 86 (Supplement C) (2015) 99 – 121. `doi:https://doi.org/10.1016/j.engstruct.2014.12.041`.

[26] P. S. Harvey, Jr., G.-P. Zéhil, H. P. Gavin, Experimental validation of simplified models for rolling isolation systems, Earthquake Engineering and Structural Dynamics 43 (2014) 1067–1088. `doi:10.1002/eqe.2387`.

[27] L.-Y. Lu, T.-Y. Lee, S.-Y. Juang, S.-W. Yeh, Polynomial friction pendulum isolators (PFPIs) for building floor isolation: An experimental and theoretical study, Engineering Structures 56 (2013) 970–982. `doi:10.1016/j.engstruct.2013.06.016`.

[28] S. Singh, S. Ramakrishna, R. Singh, Material issues in additive manufacturing: A review, Journal of Manufacturing Processes 25 (2017) 185–200. `doi:https://doi.org/10.1016/j.jmapro.2016.11.006`.

[29] D. M. Fenz, M. C. Constantinou, Spherical sliding isolation bearings with adaptive behavior: Theory, Earthquake Engineering and Structural Dynamics 37 (2008) 163–183. `doi:10.1002/eqe.751`.

[30] H. B. Mason, D. S. Hurwitz, R. K. Adams, K. Buker, R. K. Slocum, M. H. Scott, Increasing student understanding of response spectra: An argument for the inductive learning approach, Earthquake SpectraIn press. `doi:10.1193/040417EQS060O`.